Electronic Supplementary Material (ESI) for New Journal of Chemistry.
This journal is © The Royal Society of Chemistry and the Centre National de la Recherche Scientifique 2023

Electronic Supplementary Material (ESI) for New Journal of Chemistry. This journal is © The Royal Society of Chemistry 2023

Supplemental Information

Machine-learning-aided Identification of Ethanol in Humid Air Using Zinc Complex Capped $CsPbBr_3$ Quantum-dot Sensors

Yue Wang[a,c,d]‡, Xi Wang[c,e]‡, Hui Zhang[a], Shasha Gao[a], Wenjie Xu[a], Yulong Zhao[a], Mingzhi Jiao[c,e,]*, Sheng Huang[a,]* and Xiuquan Gu[a, b]*

[a] School of Materials Science and Physics, China University of Mining and Technology, Xuzhou, 221116, China.

[b] State Key Laboratory of Silicon, Zhejiang University, Hangzhou, 310027, China

[c] School of Information and Control Engineering, China University of Mining and Technology, Xuzhou 221116, China.

[d] Yuyao Sunny Intelligent Optical Technology Co., Ltd, Ningbo, 315400, P. R. China

[e] State and Local Joint Engineering Laboratory of Perception Mine, China University of Mining and Technology, Xuzhou 221116, China

† Electronic supplementary information (ESI) available. See DOI:xxxxxxx

‡ These authors contributed equally.

*These authors are corresponding authors.

To whom correspondence should be addressed:

*Dr. Xiuquan Gu

E-mail: xqgu@cumt.edu.cn

*Dr. Sheng Huang

E-mail: huangsheng@cumt.edu.cn

**Dr. Mingzhi Jiao

E-mail: mingzhijiao@cumt.edu.cn

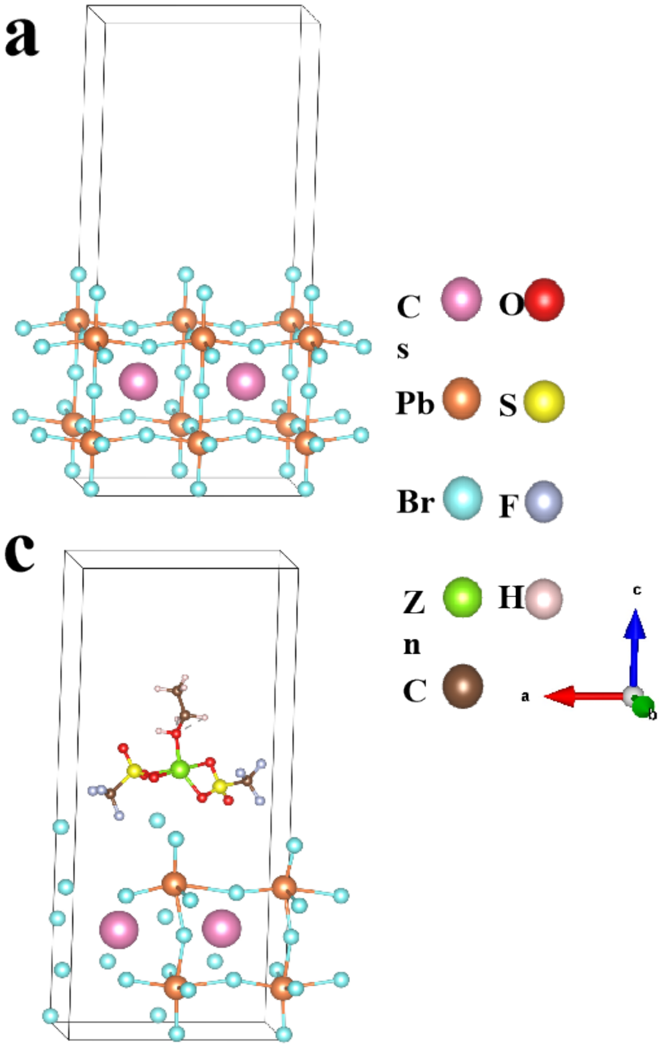

Fig. S1 Crystal structure of (a) $CsPbBr_3$ and (b) $CsPbBr_3$-Zn QDs and (c) $CsPbBr_3$-Zn QDs absorbing ethanol and (d) $CsPbBr_3$-Zn QDs absorbing H_2O. The cyan, orange, pink, purple, red, brown, yellow, silvery, green represent the atoms Cs, Pb, Br, Zn, O, C, S, F and H, respectively.

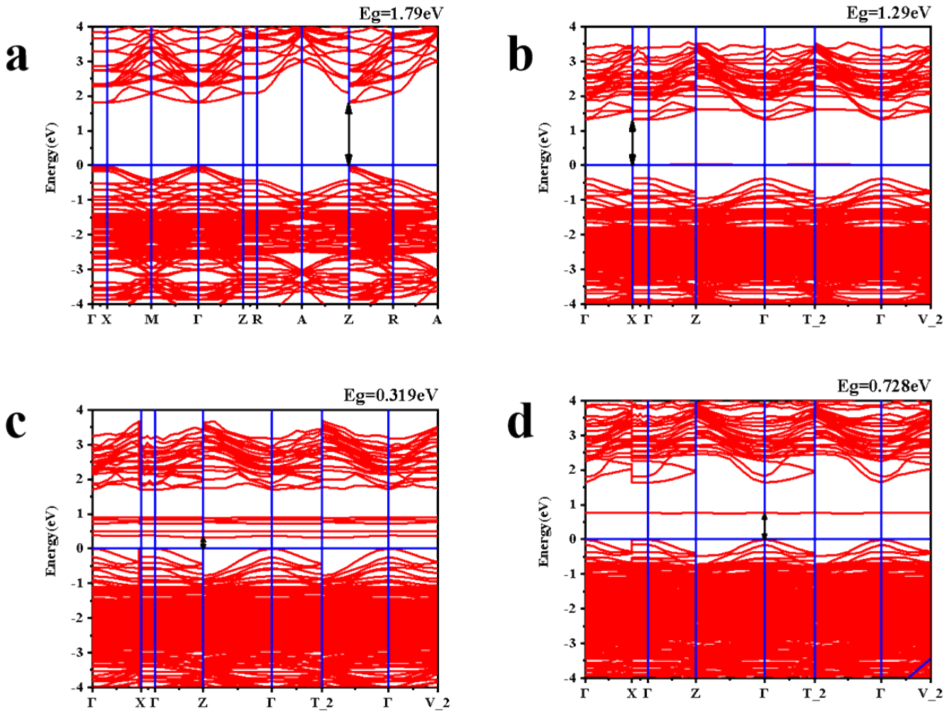

Fig. S2 DFT calculation results from Fig. S1: Energy band diagram of (a) $CsPbBr_3$ and (b) $CsPbBr_3$-Zn QDs and (c) $CsPbBr_3$-Zn QDs absorbing ethanol and (d) $CsPbBr_3$-Zn QDs absorbing H_2O.

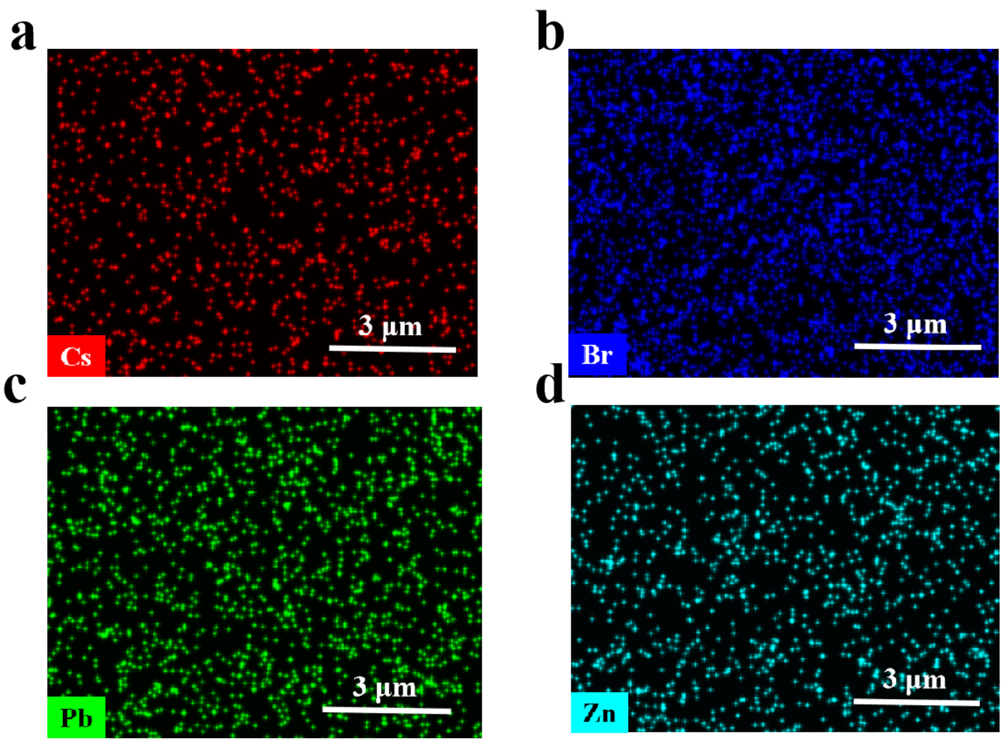

Fig. S3 Elemental mapping of Cs, Br, Pb and Zn in the $CsPbBr_3$-Zn QDs.

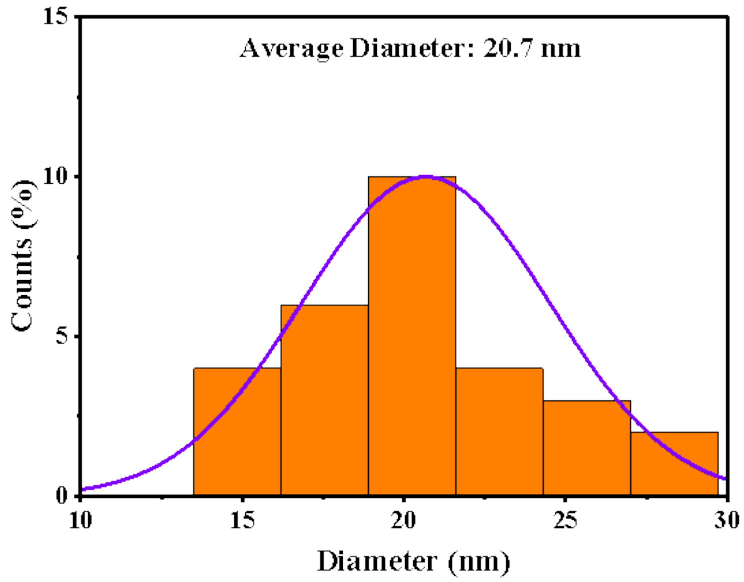

Fig. S4 Size distribution of $CsPbBr_3$-Zn QDs in Fig. 2e.

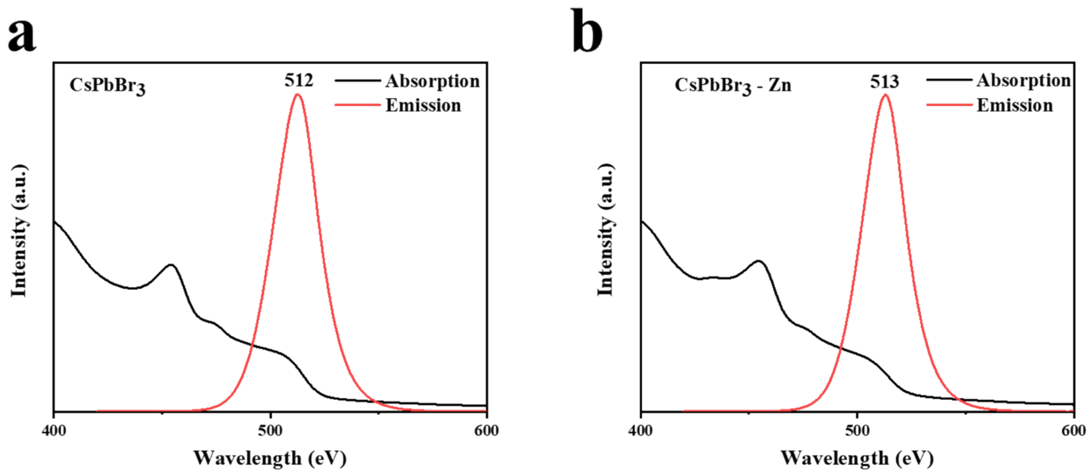

Fig. S5 PL emission and UV-vis absorption spectra of (a) $CsPbBr_3$ and (b) $CsPbBr_3$-Zn QDs.

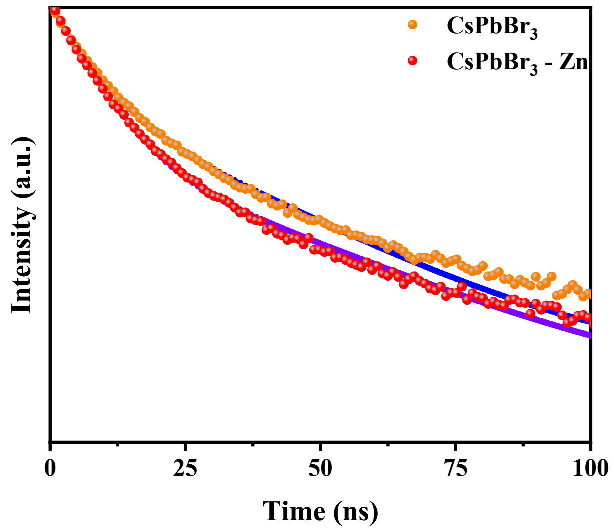

Fig. S6 Time-resolve PL delay plots of $CsPbBr_3$ (orange line) and $CsPbBr_3$-Zn QDs (red line).

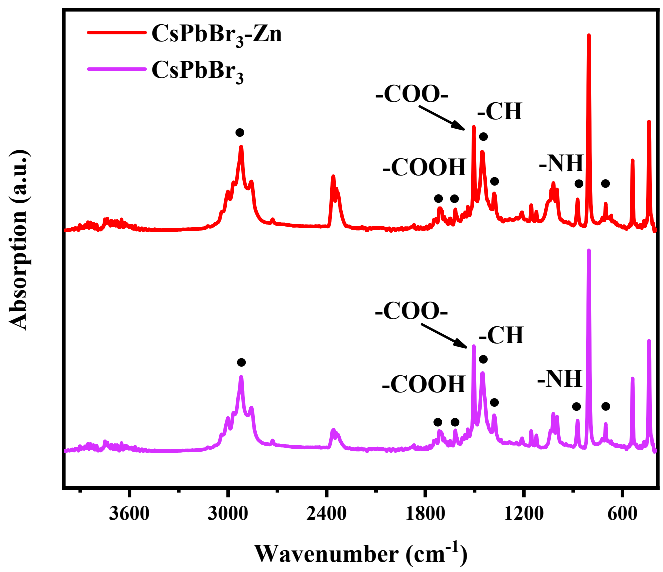

Fig. S7 Fourier transform infrared spectroscopy of $CsPbBr_3$ (purple line) and $CsPbBr_3$-Zn QDs (red line).

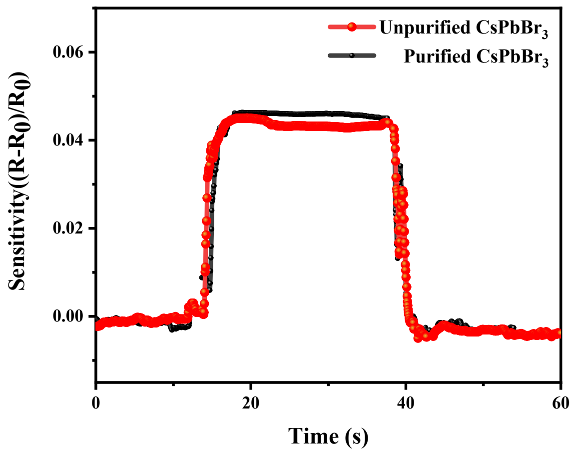

Fig. S8 Sensor responses of unpurified and purified $CsPbBr_3$ QDs towards 400 ppm ethanol at RT.

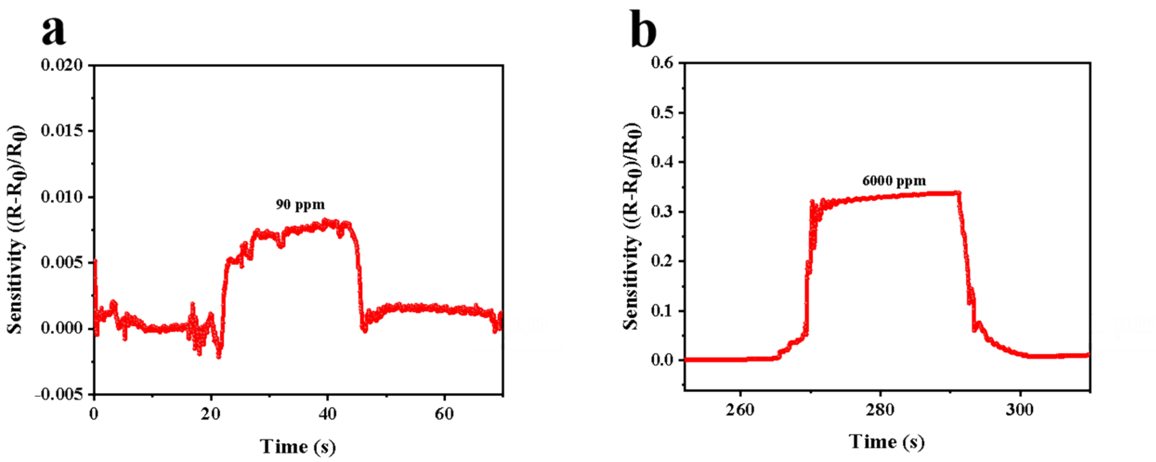

Fig. S9 (a) Lower and (b) upper detection limits of $CsPbBr_3$-Zn sensor.

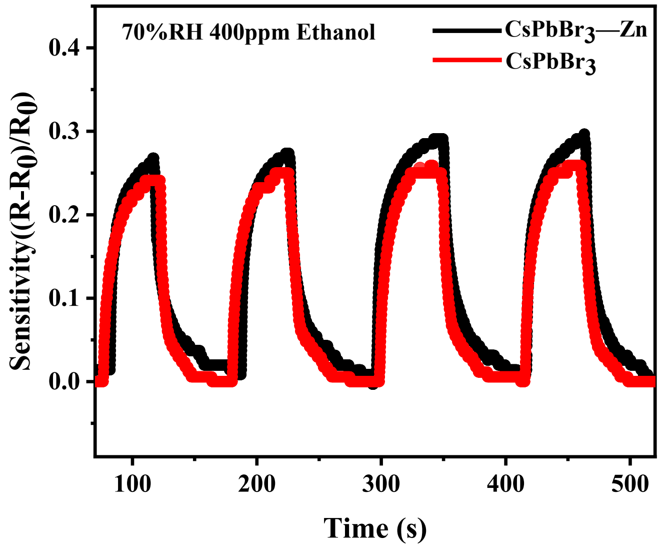

Fig. S10 Response curves of the sensors based on $CsPbBr_3$ and $CsPbBr_3$-Zn QDs under ambiance of 400 ppm ethanol and 70% RH.

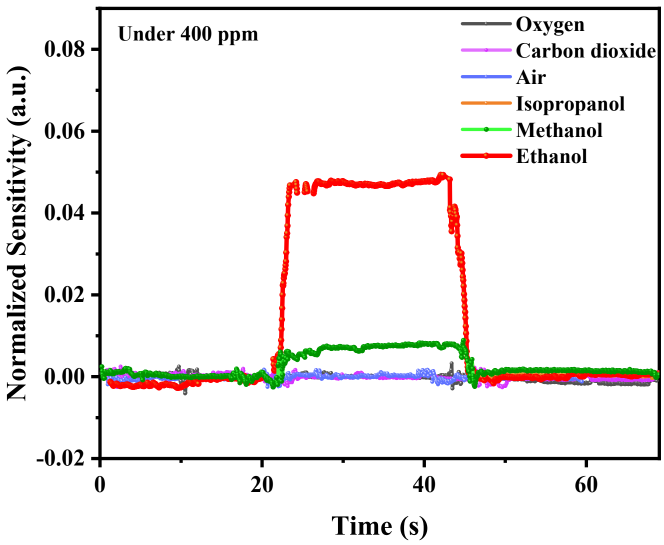

Fig. S11 Selectivity of a $CsPbBr_3$-Zn QD sensor to 400 ppm different gases (oxygen, carbon dioxide, air, isopropanol, methanol and ethanol).

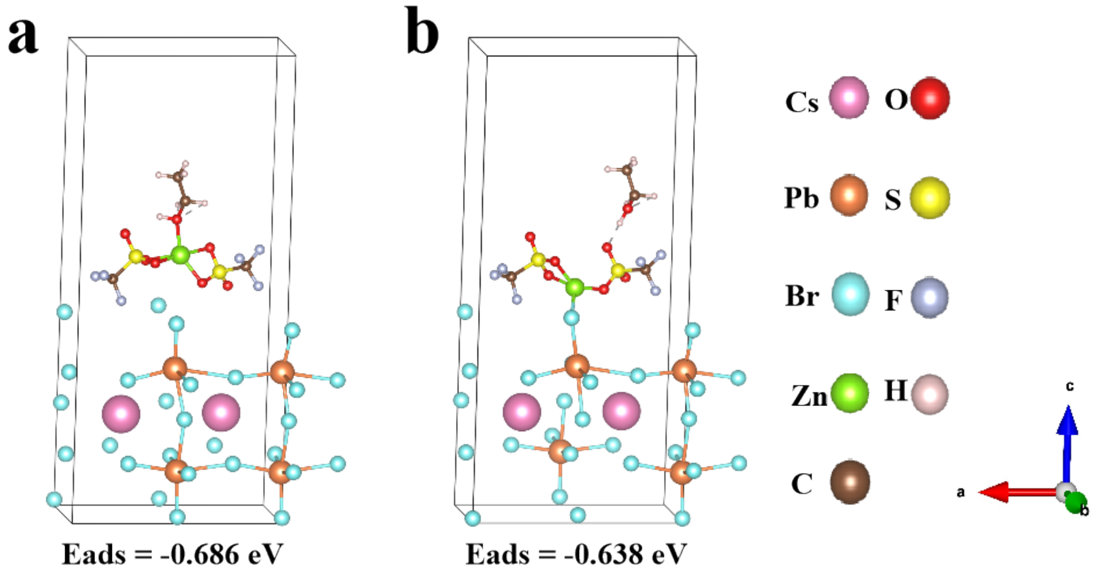

Fig. S12 Lattice model of ethanol molecule near (a) Zn atom and (b) OTf anion in the $CsPbBr_3$ crystal after coordinating with $Zn(OTf)_2$.

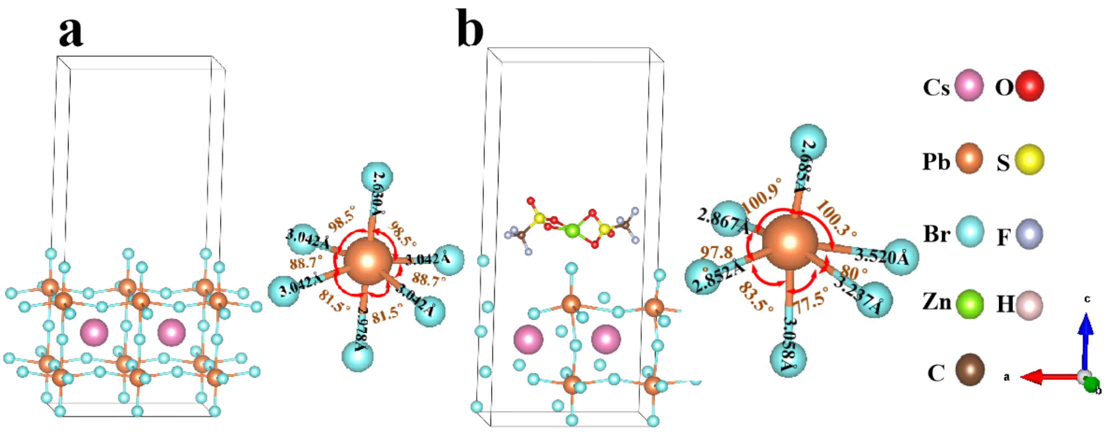

Fig. S13 Changes of bond length and bond Angle in crystal structure of $CsPbBr_3$ QDs by addition of $Zn(OTf)_2$.

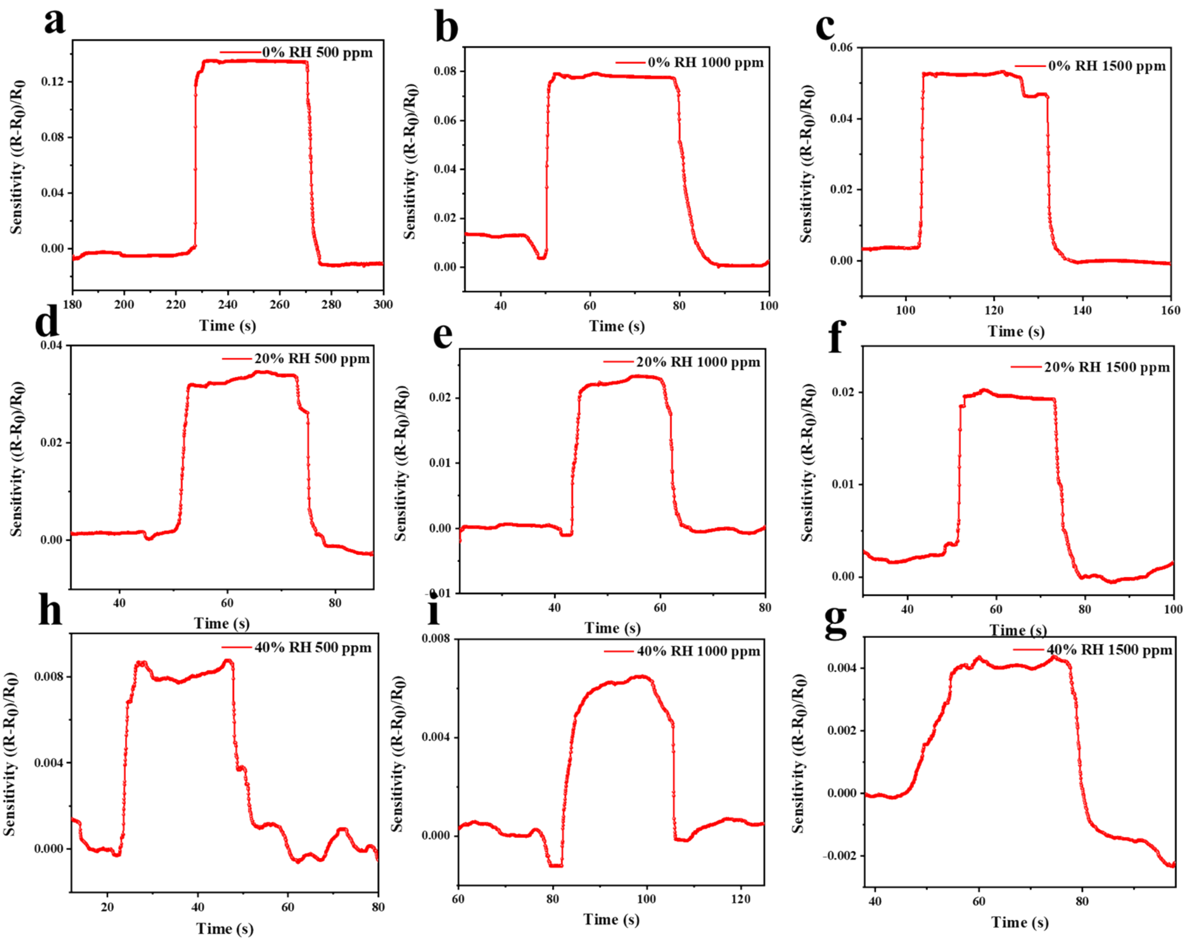

Fig. **S14** Gas response curves from a gas sensor based on $CsPbBr_3$-Zn QDs under different ethanol concentrations and relative humidity (RH) interference. (a-c) RH value = 0, (d-f) RH = 20%, (h-g) RH = 40%.

In this section, the Gramian Angular Field (GAF) method is used to convert the gas sensor response data into two-dimensional images, and the ResNet34 network [1] model is used to learn the features in the two-dimensional images, which automatically extract the features, finally realizing the recognition of 9 kinds of gas humidity and concentrations.

The specific implementation process of Gramian Angular Field is as follows: First, data is scaled for each sample data, and the data range is scaled to $[0,1]$,and the expression formula is as follows:

$$\widetilde{S}_i^t = \left[S_i^t - \min(S_i)\right] / \left[\max(S_i) - \min(S_i)\right]$$

where $\widetilde{S}_i^t$ is the normalized value at time t, S_i^t is the response value at time t, S_i and is the response value within the sampling time range. Next, the scaled normalized time series data S_i^t is converted to the polar coordinate system, that is, the value is regarded as the cosine value of the included angle, and the expression formula is as follows:

$$\theta_t = \arccos(\widetilde{S}_i^t), 0 \le \widetilde{S}_i^t \le 1.$$

Finally, Gramian angular difference field (GADF) method was used to convert the image. For the conversion of single sample time series data into GAF images, the image size is set to 64, and the single sample time series is converted into images (including GASF and GADF) as shown in Fig. S15 below.

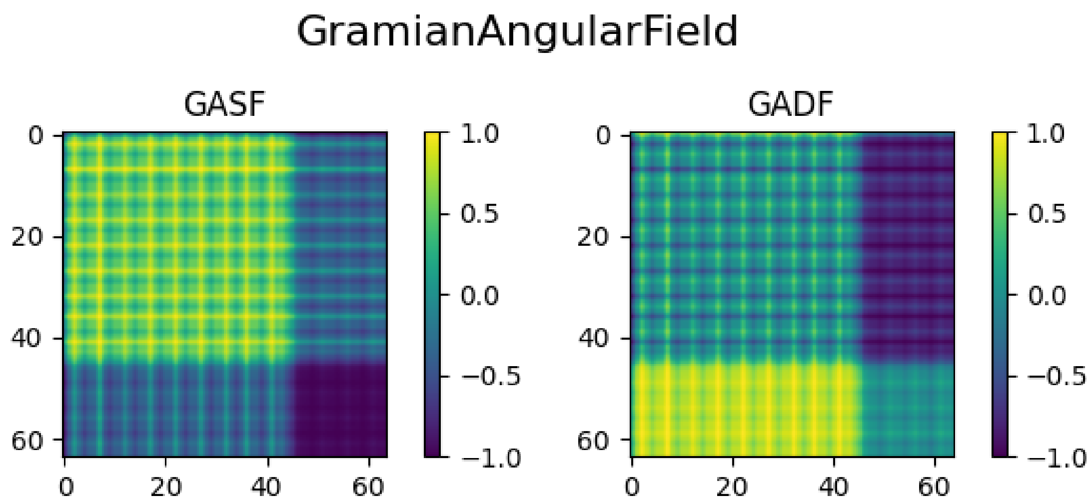

Fig. **S15** Conversion from time series data to images.

Considering the difficulty and complexity of collecting gas samples with different humidity and concentrations in the experiment, the classification network model is prone to over-fitting under small samples, so the data augmentation network strategy is adopted in this paper to increase the number of gas samples and make the classification model more robust. Data enhancement network strategies include image rotation (90°, 180° and 270°), flipping, image brightness transformation (brighter and darker), and Gaussian Blur, resulting in an 8-fold amplification of the total number of data samples in this experiment. After that, the image is input into the gas recognition network to realize the training and testing process of recognizing 9 kinds of gas humidity and concentrations. The images after data augmentation are shown in Fig. S16 below.

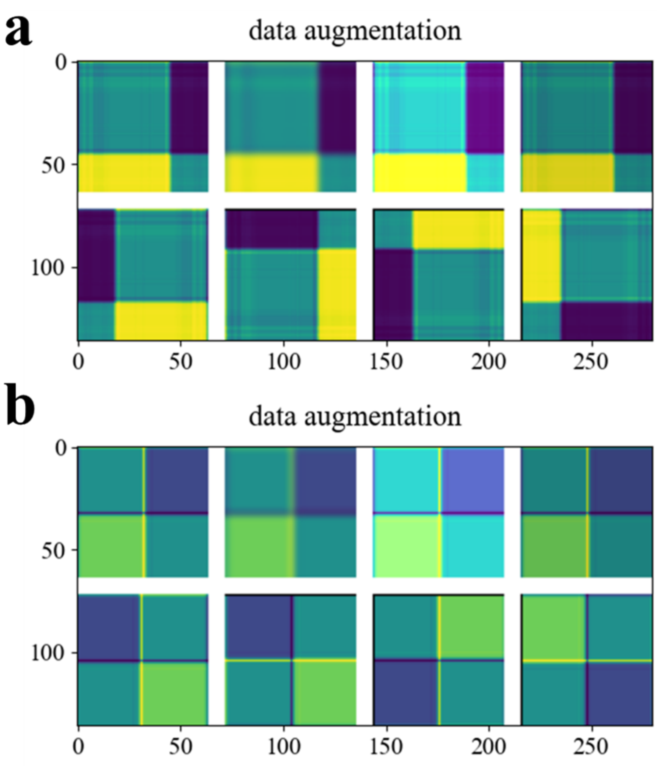

Fig. **S16** Images after data augmentation.

Table **S1** Fitted results of the PL decay of $CsPbBr_3$ and $CsPbBr_3$ – Zn QDs.

Samples	**τ_1 [ns]**	**A_1**	**τ_2 [ns]**	**A_2**	**τ_{ave} [ns]**	**λ^2**
$CsPbBr_3$ QD	3.39	0.71	13.32	0.29	9.51	0.999
$CsPbBr_3$-Zn QD	4.86	0.73	16.49	0.27	11.33	0.999

Table S2 Comparison on gas-sensing performance of $CsPbBr_3$ – Zn QDs reported in this work with the previously published articles.

Sensor	Response	T(℃)	Ethanol. Conc(ppm)	Response time (s)	Recover time (s)	Ref
$Zn(OTf)_2$	4.32%[c]	RT	400	3.9	3.6	**this work**
Ag/V_2O_5	22.5[a]	RT	500	13	7	[2]
Ga/NiO	25[b]	250	50	8	13	[3]
CuO	241%[d]	250	100	NA	NA	[4]
CuO	129%[d]	300	300	38	462	[5]
V_2O_5	81.7%[c]	280	200	17.6	39.7	[6]
ZnO/Co_3O_4	34.9[a]	300	10	57	235	[7]
PdO_x/Co_3O_4	19.6[b]	130	50	43	14	[8]
Co_3O_4/NiO	4.26[b]	250	100	NA	NA	[9]
Ag-ITO	70%[c]	130	100	45	40	[10]
In_2O_3	250[a]	250	50	16	14	[11]
Ru/WO_3	120[a]	200	100	1	18	[12]
$Pt/W_{18}O_{49}$	59[a]	300	80	20	10	[13]
In_2O_3	43.1[a]	300	100	37.6	1454.5	[14]
Sb/In_2O_3	41.3[a]	320	100	17	36	[15]
In_2O_3	180[a]	240	200	1	93	[16]
$a\text{-}MnO_2$	30.6[a]	300	200	30	40	[17]
Au/ In-Ga-Zn-O	27.9[a]	250	100	102	68	[18]
SnO_2/CuO	8.8[a]	340	250	6	10	[19]

MoS_2/TiO_2	62%[d]	350	100	52	155	[20]

a:(R_a / R_g), b:(R_g / R_a), c:([R_a - R_g] / R_a*100%), d:([R_g - R_a] / R_g*100%), NA:Not available.

References

1 A. Talapatra, U. Gajera, S. Prasad P, J. A. Chelvane, J. R. Mohanty, Understanding the magnetic microstructure through experiments and machine learning algorithms, *ACS Applied Materials & Interfaces*, 2022,**14**, 50318-50330.

2 A. H. Shah, W. Chen, Y. Liu, A. Manan, M. Hanif, I. Mehmood, F. Ahmad, Significant SRS sensing behavior of hydrothermally silver decorated sandwiched-like vanadia (Ag-V_2O_5) nanosheets toward ethanol, *Applied Physics A*, 2021, **127**, 477.

3 Shailja, K.J. Singh, Ravi Chand Singh. Highly sensitive and selective ethanol gas sensor based on Ga-doped NiO nanoparticles, *Journal of Materials Science: Materials in Electronics,* 2021, **32**, 11274-11290.

4 A. Umar, A.A. Ibrahim, H. Algadi, U.T. Nakate, S.P. Choudhury, T. Alsuwian, S. Baskoutas, Selective ethanol gas sensing performance of flower-shaped CuO composed of thin nanoplates, *Journal of Materials Science: Materials in Electronics*, 2021, **32**, 18565-18579.

5 A. Bandyopadhyay, K. Mandal, V. Ambardekar, D. Das, S.B. Majumder, Electrophoretic deposition of CuO particulate thick film for ethanol sensing, *Journal of Materials Science: Materials in Electronics*, 2021, **32**, 17324-17335.

6 I. J. Tadeo, R. Parasuraman, A. M. Umarji. Highly sensitive and selective ultrasonically nebulized V_2O_5 thin films towards ethanol and NO_2 gas detection, *Sensors and Actuators B: Chemical*, 2021, **337**, 129811.

7 T.L.H. Doan, J.Y. Kim, J.H. Lee, L.H.T. Nguyen, Y.T. Dang, K.B.T. Bui, S.S. Kim, Preparation of n-ZnO/p-Co_3O_4 heterojunctions from zeolitic imidazolate frameworks (ZIF-8/ZIF-67) for sensing low ethanol concentrations, *Sensors and Actuators B: Chemical*, 2021, **348**, 130684.

8 W. Wang, W. Jin, S. Yang, Z. Jian, W. Chen, PdO_x decorated Co_3O_4 nanosheets-assembled hollow microcages for enhanced ethanol sensing performance, *Sensors and Actuators B: Chemical*, 2021, **333**, 129583.

9 J. Gao, C. Liu, S. Guo, L. Yang, Y. Yang, X. Ku, Hetero-epitaxy growth of cobalt oxide/nickel oxide nanowire arrays on alumina substrates for enhanced ethanol sensing characteristics, *Ceramics International*, 2022, **48**, 3849-3859.

10 M. Afrouzmehr, N. Yasrebi, M.H. Sheikhi, Fabrication and characterization of Ag-Decorated indium-tin-oxide nanoparticle based ethanol sensors using an enhanced electrophoretic method, *Ceramics International*, 2021, **47**, 30504-30513.

11 C. Shen, N. Xu, R. Guan, L. Yue, W. Zhang. Highly sensitive ethanol gas sensor based on In_2O_3 spheres, *Ionics.*, 2021, **27**, 3647-3653.

12 J. Li, Q. Ding, X. Mo, Z. Zou, P. Cheng, Y. Li, D. He, A highly stable and sensitive ethanol sensor based on Ru-decorated 1D WO_3 nanowires, *RSC Advances*, 2021, **11**, 39130-39141.

13 Y. Ou, G. Zhu, W. Zhang, S. Zhang, J. Gao, H. Lu, M. Hojamberdiev. Achieving rapid response and high sensitivity in ethanol gas sensing using a $Pt/W_{18}O_{49}$ ohmic contact via modulating the adsorption and activation properties: Theoretical and experimental insights, *Sensors and Actuators B: Chemical*, 2021, **347**, 130601.

14 T.T. Liang, D.S. Kim, J.W. Yoon, Y.T. Yu, Rapid synthesis of rhombohedral In_2O_3 nanoparticles via a microwave-assisted hydrothermal pathway and their application for conductometric ethanol sensing, *Sensors and Actuators B: Chemical*, 2021, **346**, 130578.

15 X. Li, Y. Wang, P. Cheng, Y. Liu, Y. Zhang, J. Ma, C. Lv, High-performance ethanol sensor of wrinkled microspheres by spray pyrolysis, *Sensors and Actuators B: Chemical*, 2021, **344**, 130309.

16 X. Jin, Y. Li, B. Zhang, X. Xu, G. Sun, Y. Wang, Temperature-dependent dual selectivity of hierarchical porous In_2O_3 nanospheres for sensing ethanol and TEA, *Sensors and Actuators B: Chemical*, 2021, 330, 129271.

17 A. Umar, A.A. Ibrahim, R. Kumar, H. Albargi, W. Zeng, M.A.M. Alhmami, S. Baskoutas, Gas sensor device for high-performance ethanol sensing using α-MnO_2 nanoparticles, *Materials Letters*, 2021, **286**, 129232.

18 R.Y. Peng, W.C. Liu, Study of a high-performance chemoresistive ethanol gas sensor synthesized with au nanoparticles and an amorphous IGZO thin film, *IEEE Transactions on Electron Devices*, 2020, **68**, 753-760.

19 J. Zhang, S. Ma, B. Wang, S. Pei, Preparation of composite SnO_2/CuO nanotubes by electrospinning and excellent gas selectivity to ethanol, *Sensors and Actuators A: Physical*, 2021, **332**, 113090.

20 S. Singh, S. Raj, S. Sharma, Ethanol sensing using MoS_2/TiO_2 composite prepared via hydrothermal method, *Materials Today: Proceedings*, 2021, **46**, 6083-6086.